# Supporting Information

# for

## Graphene-Nanoplatelets Supported NiFe-MOF: High-Efficient and Ultra-Stable Oxygen Electrodes for Sustained Alkaline Anion Exchange Membrane Water Electrolysis

Pandiarajan Thangavel[1], Miran Ha[1,2] Shanmugasundaram Kumaraguru[3] Abhishek Meena[1], Aditya Narayan Singh[1] , Ahmad M. Harzandi[1] and Kwang S. Kim[1]*

[1]Center for Superfunctional Materials, Department of Chemistry, Ulsan National Institute of Science and Technology (UNIST), 50 UNIST-gil, Ulsan 44919, Korea.

[2]Department of Energy and Chemical Engineering, Ulsan National Institute of Science and Technology (UNIST), 50 UNIST-gil, Ulsan 44919, Korea.

[3]CSIR-Central Electrochemical Research Institute, Karaikudi-630003, Tamilnadu, India.

*E-mail: kimks@unist.ac.kr

**Supplementary Note:**

Fourier transform infrared (FTIR) spectra were obtained to analyze the surface functional groups (**Fig. 2c**). The absorption peaks at 1370 and 1427 $cm^{-1}$ corresponding to the asymmetric vibrations, while the peak at 1514 $cm^{-1}$ represents the symmetric vibrations of carboxylic group in the MOFs.[1] Similarly, a broad peak centered at 3450 $cm^{-1}$ indicating the stretching mode of OH group originates from the surface-absorbed water molecules in MOFs.[2] In addition, the peaks observed at 724 and 1313 $cm^{-1}$ are assigned to the -C-H- and C-C stretching vibrations of the benzene ring in the organic linker.[3] Peaks at 540 and 1643 $cm^{-1}$ are attributed to bond between metal ions and COO- groups of BTC, which reveals the successful coordination of Ni/Fe with the BTC linker.[4-6]

The surface characteristics of NiFe-BTC-GNPs are also evaluated using Raman spectroscopy (**Fig. 2d**). All MOF samples exhibit characteristic Raman active mode at 1000 and 3085 $cm^{-1}$ corresponding to ν(CH) stretching of the organic linker[7]. Similarly, the bands at 1610 and 1006 $cm^{-1}$ are related to ν(C=C) modes of the benzene ring; the peaks at 824 and 724 $cm^{-1}$ are attributed to out-of-plane ring (C−H) bending vibrations and out-of-plane ring bending, respectively. Further, the doublet located at 1550 and 1460 $cm^{-1}$ indicate the presence of asym($C-O_2$) and asym($C-O_2$) groups.[8] In the case of NiFe-BTC-GNPs and NiFe-BTC MOFs, three additional bands at 480, 565 and 719 $cm^{-1}$ are assigned to the characteristic bands of M-O-M and M-O (M=$Ni^{2+}$/ $Fe^{3+}$) in the corresponding MOF.[9, 10] These results are consistent with FTIR-spectral data in **Fig. 2c**. Particularly, the absence of the COOH peak around 1760–1690 $cm^{-1}$ would be a direct evidence of metal coordination with BTC.[4-6] Furthermore, the Raman spectra of NiFe-BTC-GNPs displays the major Raman features of graphene at 1350, 1582 and 2708 $cm^{-1}$ corresponding to D, G and 2D bands, respectively. The appearance of low-intensity D band indicates the high quality of the graphene in NiFe-BTC-GNPs. Besides, the sharp narrow 2D band

along with an $I_{2D}/I_G$ value of 5.0 implies the presence of few-layer graphene in the composite material.[11, 12]

**Supplementary Figures**

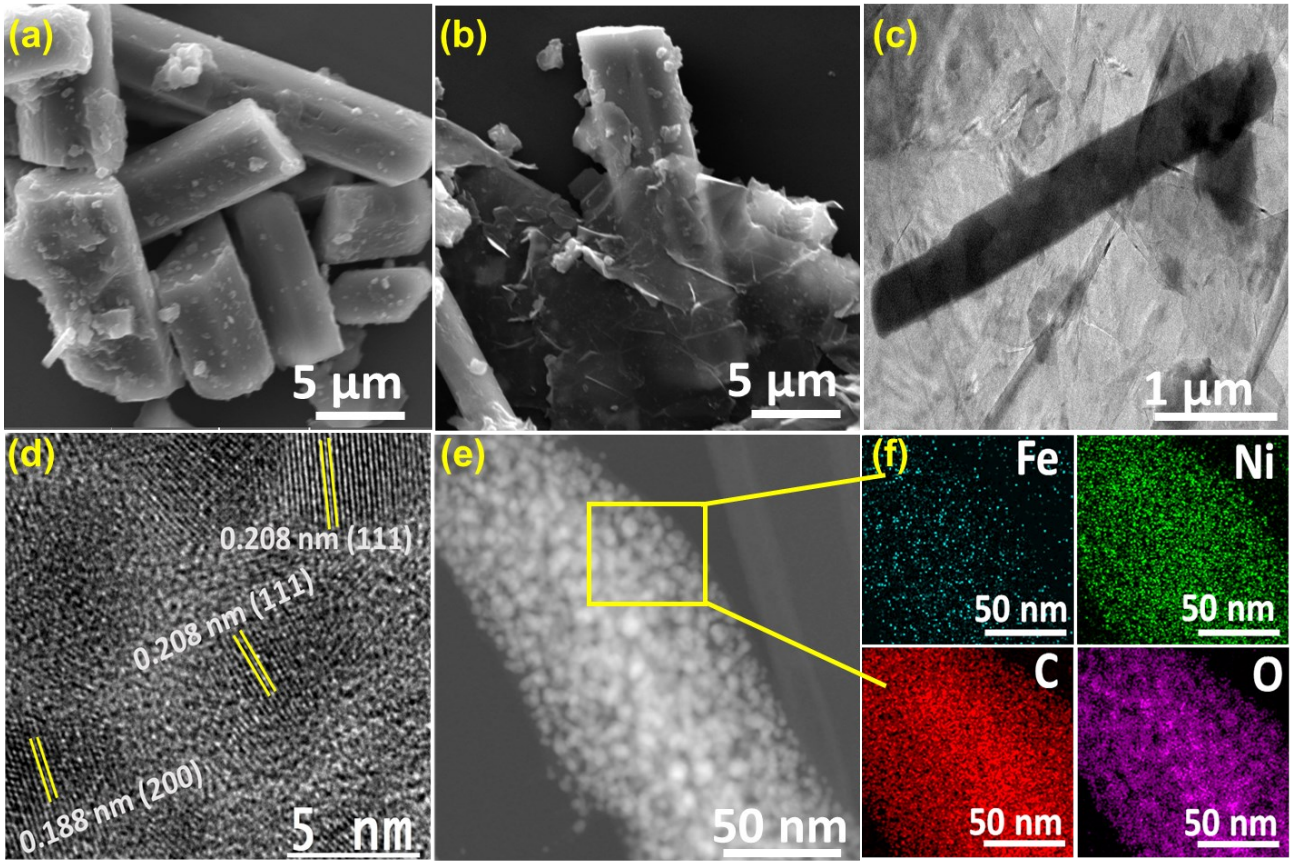


**Fig. S1** SEM and HRTEM images of NiFe-BTC and NiFe-BTC-GNPs MOFs. a**,** SEM images of NiFe-BTC. **b-d,** SEM (b,c) and HRTEM (d) images of NiFe-BTC-GNPs. **f,** HRTEM-EDS mapping of NiFe-BTC-GNPs.

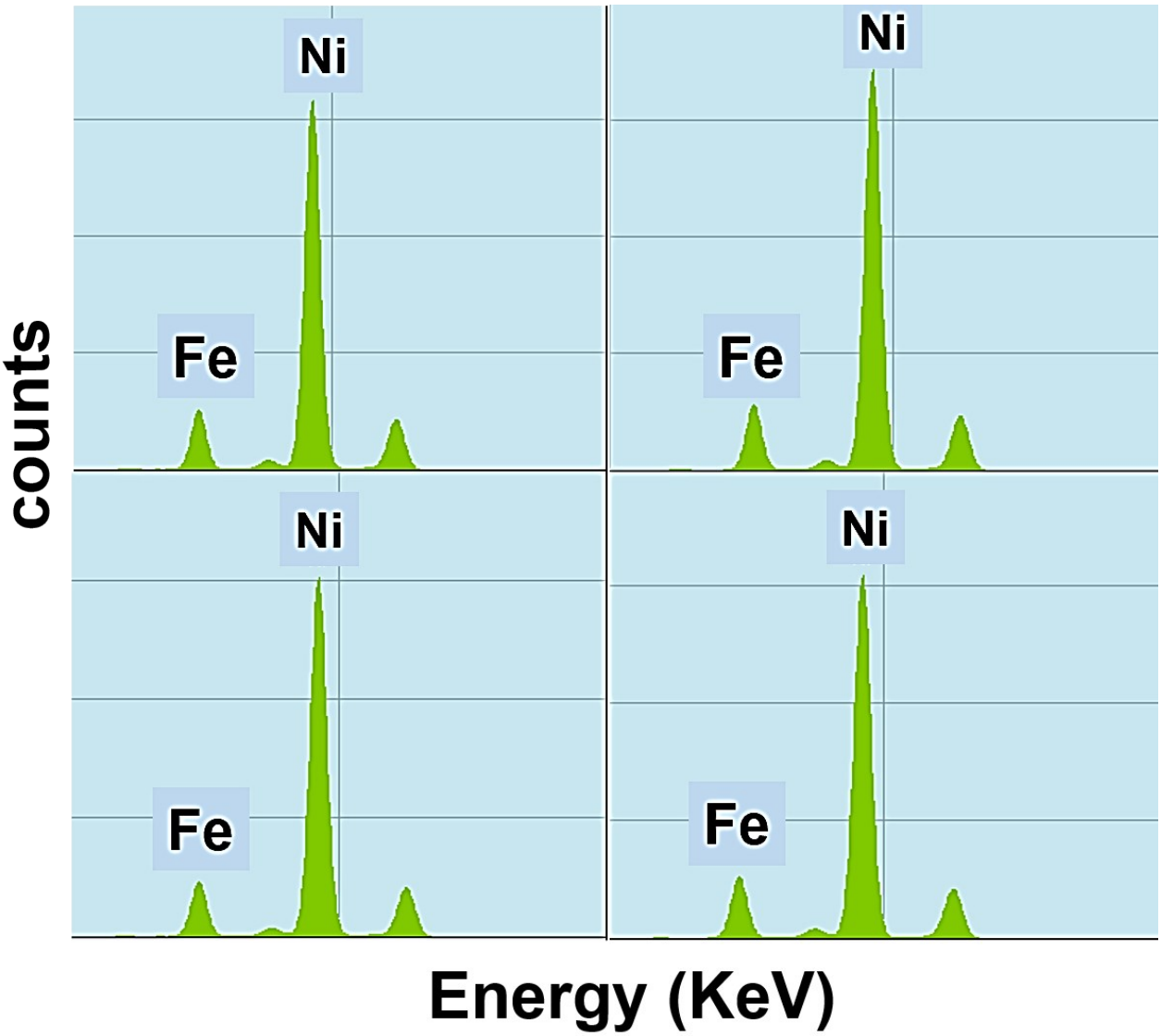


**Fig. S2** Elemental analysis Of NiFe-BTC-GNPs MOF. EDAX-XRF Analysis of NiFe-BTC-GNPs at different locations.

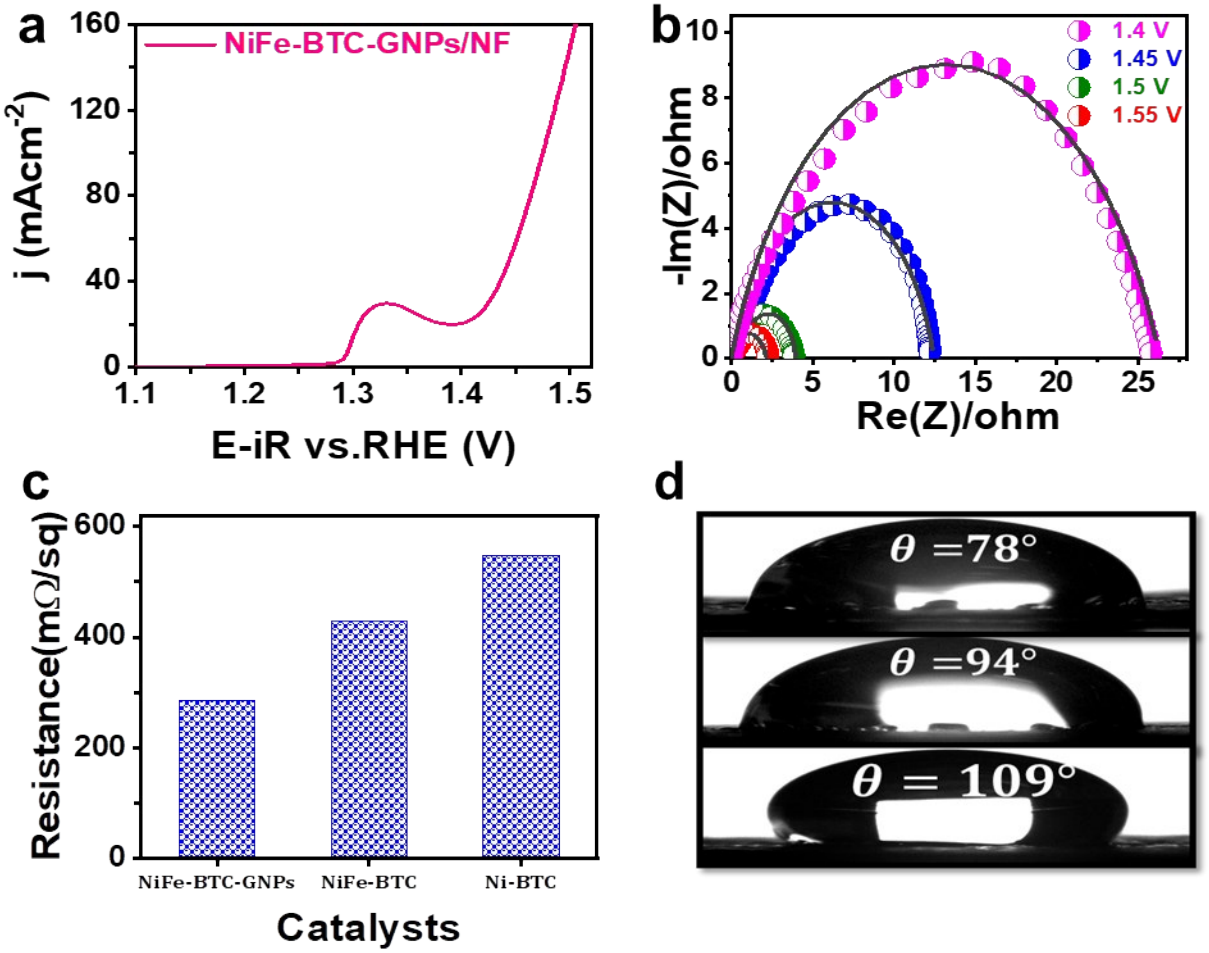


**Fig. S3** Electrochemical and Physical characterization of the MOF samples. **a,** Polarization curves of the NiFe-BTC-GNPs MOF loaded on Nickel Foam (NF) in 1M KOH Solution. **b,** Nyquist plots of NiFe-BTC-GNPs electrode measured as a function of applied potential in 1M KOH solution. **c,** Four Point Probe analysis of MOF samples. **d,** Contact angle measurements of the MOF samples (from bottom to top: Ni-BTC, NiFe-BTC, and NiFe-BTC-GNPs MOF).

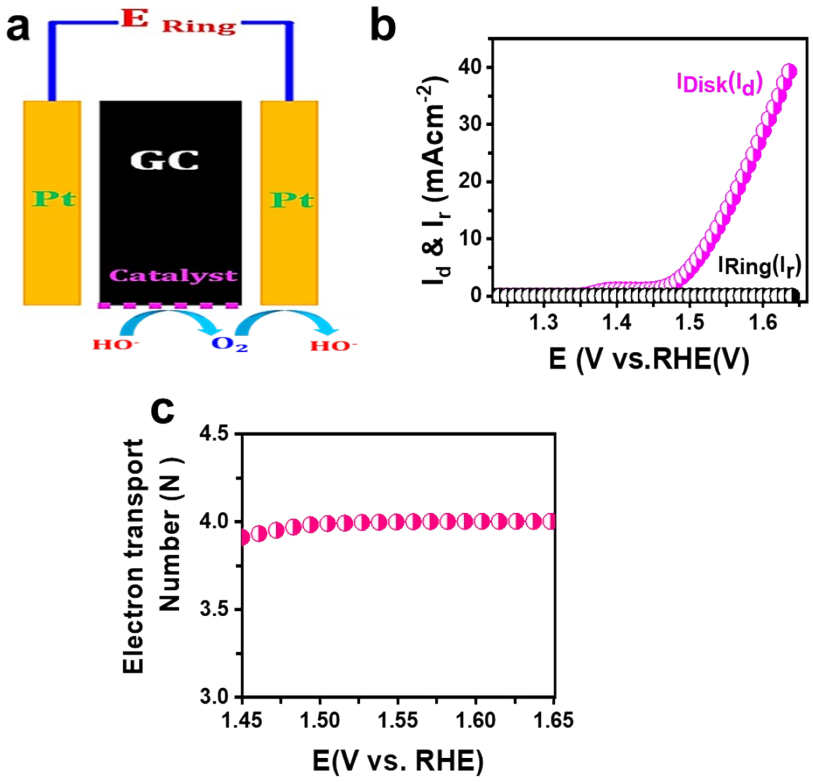


**Fig. S4** Faradaic efficiency calculation measured through ORR-OER method **a,** RRDE Setup. **b,** Rotating ring disk electrode (RRDE) voltammogram of NiFe-BTC-GNPs. **C,** Electron-transfer number (n) as a function of applied potential calculated from fig.b.

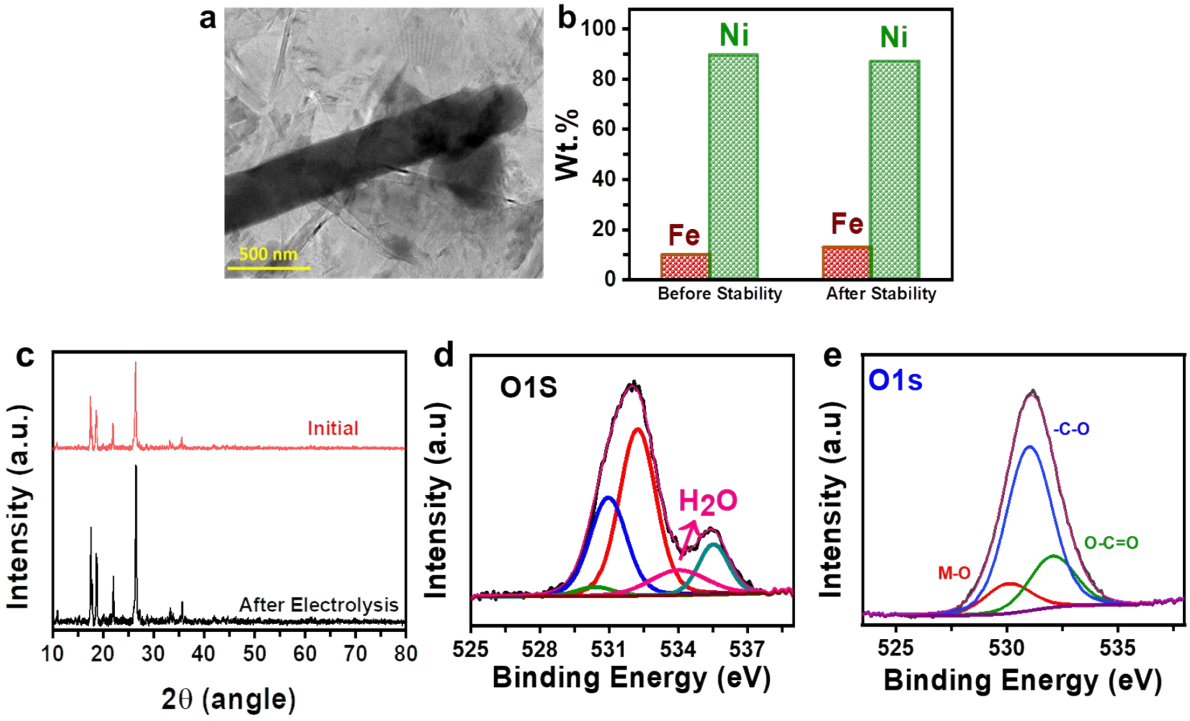


**Fig. S5** Elemental and crystal Phase analysis of NiFe-BTC-GNPs MOF after long-term stability studies. **a,** HRTEM image of NiFeBTC-GNPs after continuous electrolysis. **b,** ICP-MS analysis as – prepared sample and after stability. **c,** XRD Pattern of NiFe-BTC-GNPs. **d,e,** High-resolution O1S spectra of NiFe-BTC-GNPs MOF (d) after and (e) before continuous electrolysis.

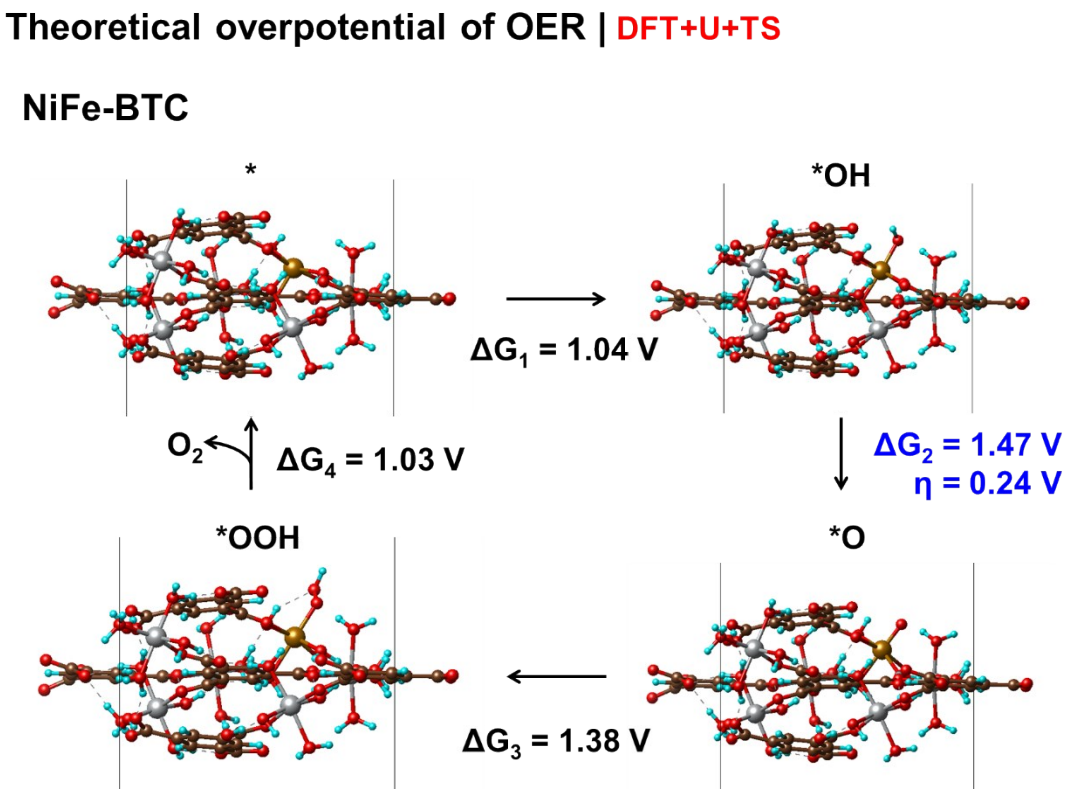


**Fig. S6** DFT-predicted structures of each intermediates on the active sites, their free energy differences and overpotentials. Fe site of NiFe-BTC (Fe: yellow, Ni: grey, C: brown, O: red, and H: cyan, respectively).

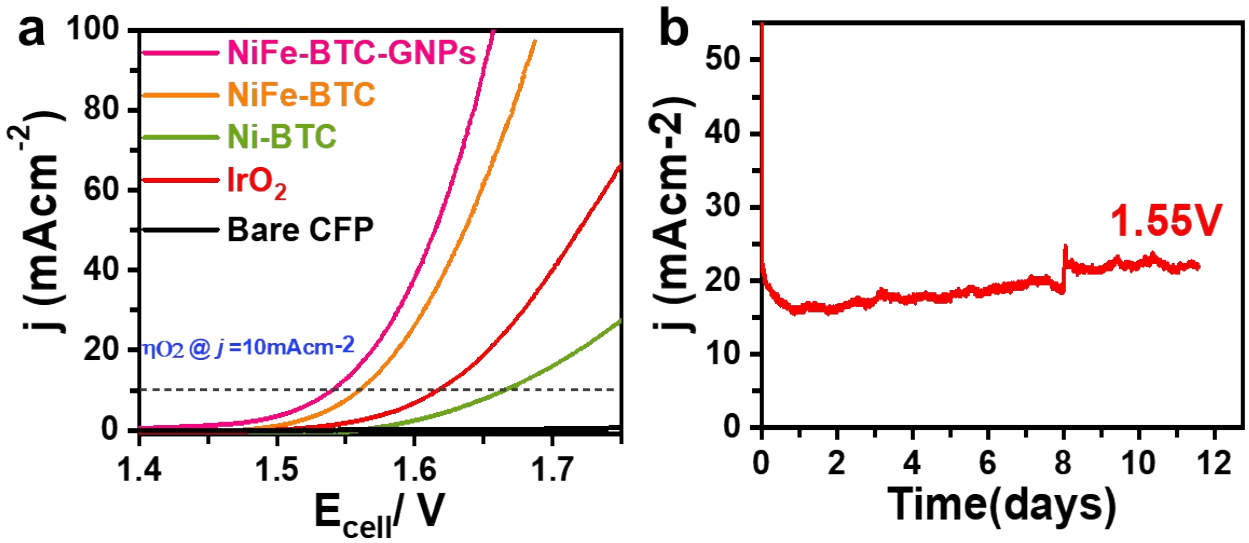


**Fig. S7** OER activity of MOF in Conventional Electrolyser: OER Performance of MOF measured in the conventional electrolyser using 20 wt% Pt/C as a cathode**. a,** Polarization plots of the electrolyser obtained in 1M aqueous KOH solution at RT with scan rate of 1mV $S.^{-1}$ **b,** Long-term stability of the electrolyser with NiFe-BTC-GNPs anode measured by applying a constant potential of 1.55 V for 12 days. The conventional electrolyser (fine frit-separator) was fabricated by utilizing the as-synthesized BTC-derived catalysts on CFP as anode electrodes and the commercial 20% Pt/C on CFP as cathode electrodes. For comparison, the state-of-the-art $IrO_2$ and $Co_3O_4$ based anodes were also fabricated. NiFe-BTC-GNPs based electrolyzer exhibits excellent performance compared to other anode catalysts, requiring smaller η=250/330mV to reach j=10/100 mA $cm^{-2}$ (a). These values are even better than the state-of-the-art $IrO_2$/(Pt/C) electrodes which demands larger η to achieve similar current densities. The NiFe-BTC-GNPs based electrolyser demonstrates excellent long-term stability for 12 days on continuous electrolysis operation (b).

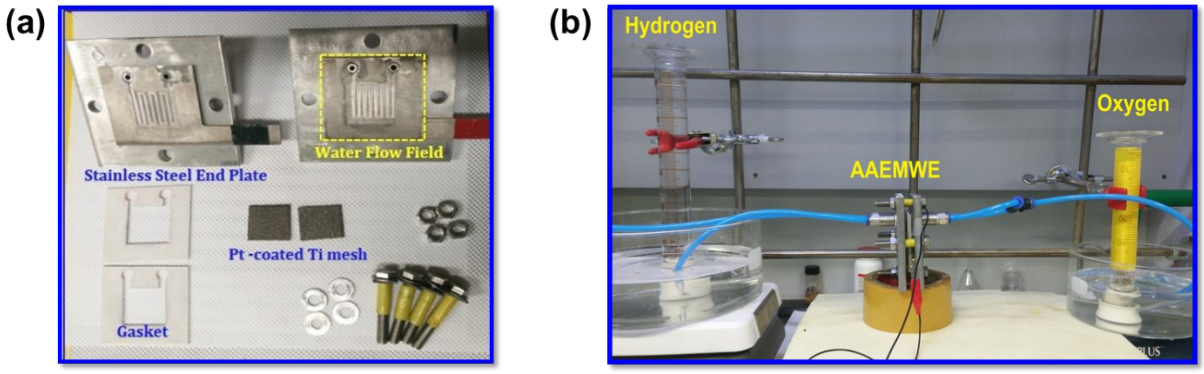


**Fig. S8** Components of Prototype AAEMWE . (a) AAEMWE setup used in this study. (b) Demonstration of AAEMWE for practical hydrogen generation.

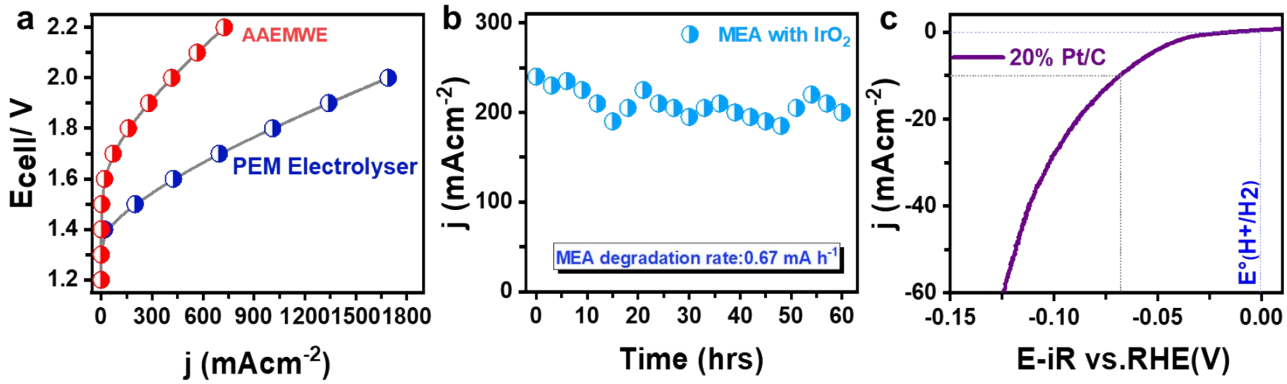


**Fig. S9** Electrochemical characterization of Commercial AAEMWE **a,** LSV curves of AAEMWE and PEM electrolyser with Commercial 20% Pt/C cathode and $IrO_2$ anode in ultrapure water electrolyte at 70℃. **b,** Stability of MEA with commercial catalysts (20 % Pt/C cathode and $IrO_2$ anode) at 25℃.**c,** Polarization curve obtained with commercial Pt/C loaded on CFP in 1M KOH solution.

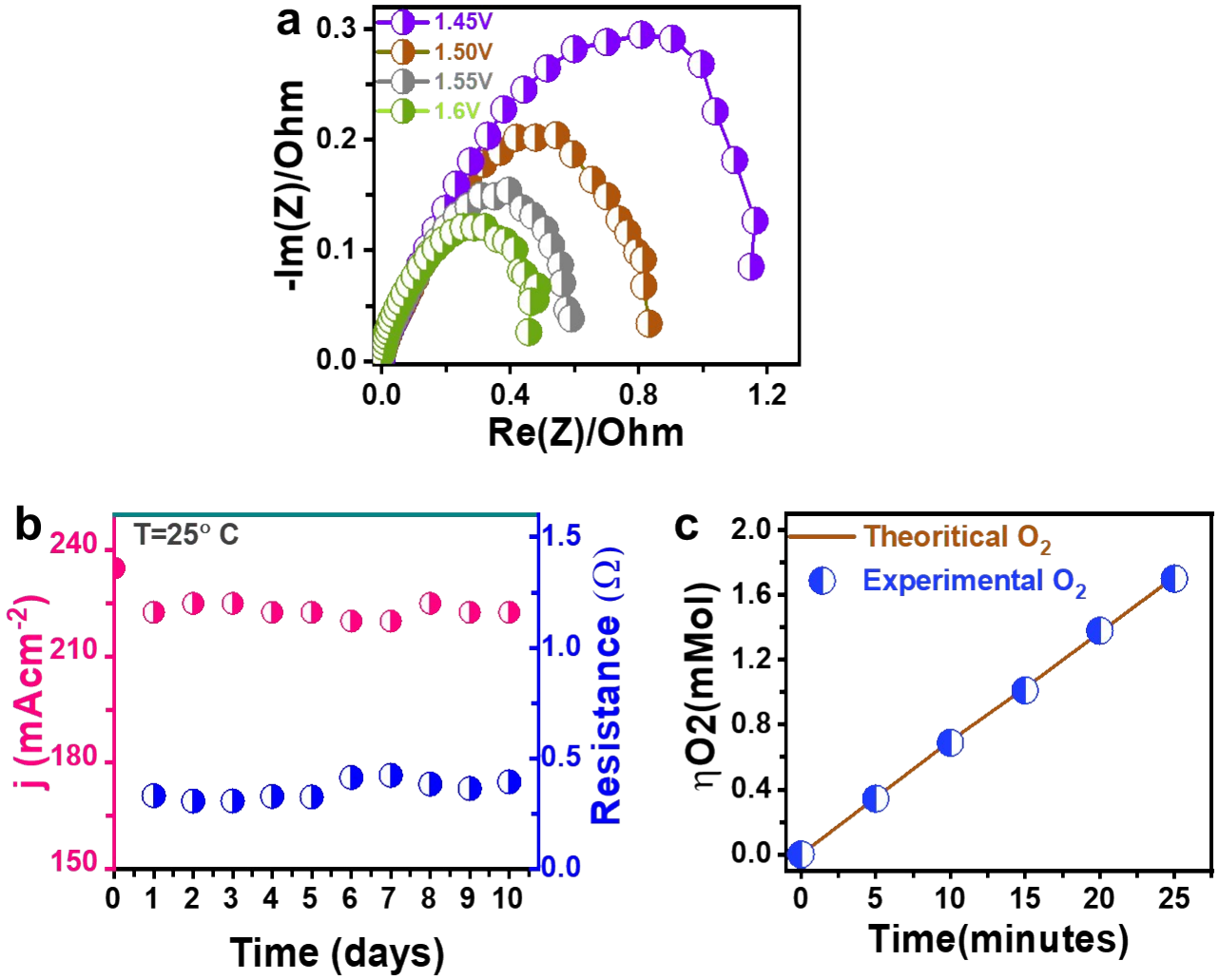


**Fig. S10** Electrochemical characterization of NiFe-BTC-GNPs based AAEMWE **a,** Nyquist plots of AEM water electrolyser measured as a function of applied potential in the ultra-pure water. **b,** Long-term durability of the cell with pt/C cathode at constant potential 1.8 V. **c,** Faradaic efficiency measured through water displacement method.

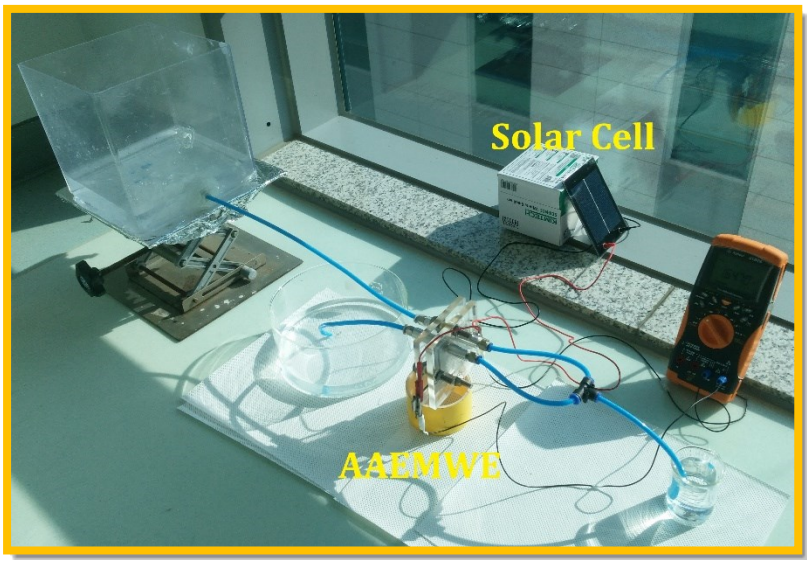


**Fig. S11** Solar-to-hydrogen (STH) conversion: Demonstration of PV-powered AAEMWE for solar hydrogen production. Experimental set up used for the Solar to Hydrogen Efficiency (STH) Measurements. The single cell comprising NiFe-BTC-GNPs MOF as anode catalyst was integrated with commercial silicon solar cell.

## Supplementary Tables

**Table S1.** Summary of the OER performance of our catalysts compared with high performance catalysts reported in the literature.

| Catalysts | Electrolyte | $\eta O_2$ @ j=10 mA $cm^{-2}$ (mV) | Stability (hrs) | Reference |
|---|---|---|---|---|
| NiFe-BTC-GNPs MOF/CFP | 1M KOH | 220 | 1000* | This work |
| NiFe-BTC-GNPS MOF/NF | 1M KOH | 180 (j=20) | | This Work |
| NiFeLDH/NF | 1M KOH | 250 | 96 | This work |
| $IrO_2$/CFP | 1M KOH | 280 | 32 | This Work |
| Ultrathin Nico-MOF/NF | 1M KOH | 189 | 11 | 13 |
| Ultrathin NiFe-MOF/NF | 1M KOH | 240 | 5.5 | 14 |
| Fe1Ni2-BDC MOF/GCE | 1M KOH | 260 | 10 | 3 |
| Co0.6Fe0.4-MOF-74/GCE | 1M KOH | 280 | 12 | 15 |
| $NaNi_{0.8}Fe_{0.2}O_2$ | 1M KOH | 320 | 30 | *16* |
| $O_2$-Cat-1/Fe Plate | 1M KOH | 269 | 100 | 17 |
| NiFe hydroxide/ Nickel Foam | 1M KOH | 245 | 10 | 18 |
| NiFe LDH/Nickel Foam | 1M KOH | 240 | 10 | 19 |
| Ni–Co–P Hollow Nano bricks | 1M KOH | 270 | 20 | 20 |
| cobalt-vanadium hydr(oxy)oxide | 1M KOH | 250 | 170 | 21 |
| $Ni_{0.75}V_{0.25}$-LDH | 1M KOH | 320 | 25 | 22 |

Some of the information was not specified in the literature and was estimated according to the data graphs.

CFP: Carbon Fiber Paper , NF: Nickel Foam

GCE : Glassy carbon electrode

*Overall stability : cv cycles, half-cell stability and electrolyser stability

**References:**


1. W. J. Li, S. Watzele, H. A. El-Sayed, Y. C. Liang, G. Kieslich, A. S. Bandarenka, K. Rodewald, B. Rieger and R. A. Fischer, *Journal of the American Chemical Society*, 2019, **141**, 5926-5933.
2. Q. Sun, M. Liu, K. Li, Y. Han, Y. Zuo, F. Chai, C. Song, G. Zhang and X. Guo, *Inorganic Chemistry Frontiers*, 2017, **4**, 144-153.
3. J. Li, W. Huang, M. Wang, S. Xi, J. Meng, K. Zhao, J. Jin, W. Xu, Z. Wang, X. Liu, Q. Chen, L. Xu, X. Liao, Y. Jiang, K. A. Owusu, B. Jiang, C. Chen, D. Fan, L. Zhou and L. Mai, *ACS Energy Letters*, 2018, **4**, 285-292.
4. O. M. Yaghi, H. Li and T. L. Groy, *Journal of the American Chemical Society*, 1996, **118**, 9096-9101.
5. L. T. L. Nguyen, T. T. Nguyen, K. D. Nguyen and N. T. S. Phan, *Applied Catalysis A: General*, 2012, **425-426**, 44-52.
6. C. E. Santolalla-Vargas, V. Santes, C. Ortega-Niño, A. Hernández-Gordillo, F. Sanchez-Minero, L. Lartundo-Rojas, R. Borja-Urby, J. C. López-Curiel, O. Goiz and I. I. Padilla-Martinez, *Catalysis Today*, 2018, DOI: 10.1016/j.cattod.2018.02.010.
7. Y. Kim, K. Cho, K. Lee, J. Choo, M.-s. Gong and S.-W. Joo, *Journal of Molecular Structure*, 2008, **878**, 155-161.
8. C. Prestipino, L. Regli, J. G. Vitillo, F. Bonino, A. Damin, C. Lamberti, A. Zecchina, P. L. Solari, K. O. Kongshaug and S. Bordiga, *Chemistry of Materials*, 2006, **18**, 1337-1346.
9. L. Cai, J. Zhao, H. Li, J. Park, I. S. Cho, H. S. Han and X. Zheng, *ACS Energy Letters*, 2016, **1**, 624-632.
10. M. W. Louie and A. T. Bell, *Journal of the American Chemical Society*, 2013, **135**, 12329-12337.
11. J. B. Wu, M. L. Lin, X. Cong, H. N. Liu and P. H. Tan, *Chem Soc Rev*, 2018, **47**, 1822-1873.
12. M. Jahan, Q. Bao and K. P. Loh, *Journal of the American Chemical Society*, 2012, **134**, 6707-6713.
13. S. Zhao, Y. Wang, J. Dong, C.-T. He, H. Yin, P. An, K. Zhao, X. Zhang, C. Gao, L. Zhang, J. Lv, J. Wang, J. Zhang, A. M. Khattak, N. A. Khan, Z. Wei, J. Zhang, S. Liu, H. Zhao and Z. Tang, *Nature Energy*, 2016, **1**.
14. J. Duan, S. Chen and C. Zhao, *Nature Communications*, 2017, **8**, 15341.

15. X. Zhao, B. Pattengale, D. Fan, Z. Zou, Y. Zhao, J. Du, J. Huang and C. Xu, *ACS Energy Letters*, 2018, **3**, 2520-2526.
16. B. Weng, F. Xu, C. Wang, W. Meng, C. R. Grice and Y. Yan, *Energy & Environmental Science*, 2017, **10**, 121-128.
17. Y. Liu, X. Liang, L. Gu, Y. Zhang, G. D. Li, X. Zou and J. S. Chen, *Nature Communications*, 2018, **9**, 2609.
18. X. Lu and C. Zhao, *Nature Communications*, 2015, **6**, 6616.
19. J. Luo, J.-H. Im, M. T. Mayer, M. Schreier, M. K. Nazeeruddin, N.-G. Park, S. D. Tilley, H. J. Fan and M. Grätzel, *Science*, 2014, **345**, 1593.
20. E. Hu, Y. Feng, J. Nai, D. Zhao, Y. Hu and X. W. Lou, *Energy & Environmental Science*, 2018, **11**, 872-880.
21. J. Liu, Y. Ji, J. Nai, X. Niu, Y. Luo, L. Guo and S. Yang, *Energy & Environmental Science*, 2018, **11**, 1736-1741.
22. K. Fan, H. Chen, Y. Ji, H. Huang, P. M. Claesson, Q. Daniel, B. Philippe, H. Rensmo, F. Li, Y. Luo and L. Sun, *Nature Communications*, 2016, **7**, 11981.